Materials Advances

ROYAL SOCIETY OF CHEMISTRY

PAPER

View Article Online
View Journal | View Issue

Cite this: *Mater. Adv.*, 2021, 2, 2299

Electrochemical behavior of a Ni_3N OER precatalyst in Fe-purified alkaline media: the impact of self-oxidation and Fe incorporation†

Kenta Kawashima, [a] Raúl A. Márquez-Montes, [a] Hao Li,[ab] Kihyun Shin, [ab] Chi L. Cao,[c] Kobe M. Vo, [c] Yoon Jun Son,[c] Bryan R. Wygant,[a] Adithya Chunangad,[c] Duck Hyun Youn, [d] Graeme Henkelman,[ab] Víctor H. Ramos-Sánchez [e] and C. Buddie Mullins [*acfg]

Nickel nitride (Ni_3N) is known as one of the promising precatalysts for the electrochemical oxygen evolution reaction (OER) under alkaline conditions. Due to its relatively low oxidation resistance, Ni_3N is electrochemically self-oxidized into nickel oxides/oxyhydroxides (electroactive sites) during the OER. However, we lack a full understanding of the effects of Ni_3N self-oxidation and Fe impurity incorporation into Ni_3N from electrolyte towards OER activity. Here, we report on our examination of the compositional and structural transformation of Ni_3N precatalyst layers on Ni foams (Ni_3N/Ni foam) during extended periods of OER testing in Fe-purified and unpurified KOH media using both a standard three-electrode cell and a flow cell, and discuss their electrocatalytic properties. After the OER tests in both KOH media, the Ni_3N surfaces were converted into amorphous, nano-porous nickel oxide/(oxy)hydroxide surfaces. In the Fe-purified electrolyte, a decrease in OER activity was confirmed after the OER test because of the formation of pure NiOOH with low OER activity and electrical conductivity. Conversely, in the unpurified electrolyte, a continuous increase in OER activity was observed over the OER testing, which may have resulted from the Fe incorporation into the self-oxidation-formed NiOOH. Our experimental findings revealed that Fe impurities play an essential role in obtaining notable OER activity using the Ni_3N precatalyst. Additionally, our Ni_3N/Ni foam electrode exhibited a low OER overpotential of 262 mV to reach a geometric current density of 10 mA cm_{geo}^{-2} in a flow cell with unpurified electrolyte.

Received 12th February 2021,
Accepted 28th February 2021

DOI: 10.1039/d1ma00130b

rsc.li/materials-advances

Introduction

Hydrogen production from electrocatalytic overall water splitting, which consists of the hydrogen evolution reaction (HER) and the oxygen evolution reaction (OER), is a promising green technology for future energy conversion and storage. The sluggish kinetics of the OER, the result of multiple electron transfers and chemical intermediates (*i.e.*, HO*, O*, and HOO*), acts as a bottleneck for water splitting and dominates the overall efficiency of this technology.[1] To speed up the OER and make large-scale water splitting practical, an earth-abundant, highly efficient, and durable electrocatalytic material is highly desirable and urgently necessary. In recent years, transition metal borides, carbides, pnictides, and chalcogenides, all of which we will refer to here as "TM X-ides", have drawn considerable attention as viable oxygen evolution electrocatalysts.[2–9] Except for some special cases (*e.g.*, FeP, Ni_3Se_2, and Ni_3Te_2),[10–12] most TM X-ides are self-oxidized into their TM oxide/(oxy)hydroxide counterparts under potentials at which OER occurs.[13–20] As the newly-formed TM oxide/(oxy)hydroxide species are more favorable electrocatalytic active sites for the OER than the

[a] *Department of Chemistry, The University of Texas at Austin, Austin, Texas 78712, USA. E-mail: mullins@che.utexas.edu*
[b] *Oden Institute for Computational Engineering and Sciences, The University of Texas at Austin, Austin, Texas 78712, USA*
[c] *McKetta Department of Chemical Engineering, The University of Texas at Austin, Austin, Texas 78712, USA*
[d] *Department of Chemical Engineering, Interdisciplinary Program in Advanced Functional Materials and Devices Development, Kangwon National University, Chuncheon, Gangwon-do 24341, South Korea*
[e] *Facultad de Ciencias Químicas, Universidad Autónoma de Chihuahua, Chihuahua, Chihuahua 7 31125, Mexico*
[f] *Center for Electrochemistry, The University of Texas at Austin, Austin, Texas 78712, USA*
[g] *H2@UT, The University of Texas at Austin, Austin, Texas 78712, USA*

† Electronic supplementary information (ESI) available: Experimental details, digital photographs, schematic illustrations, electrochemical stability map, additional XRD, SEM, EDX, and XPS results, and cyclic voltammograms. See DOI: 10.1039/d1ma00130b

initial TM X-ide, these easily oxidizable TM X-ides are sometimes described as "precatalysts".[17] Moreover, the TM oxides/(oxy)hydroxides derived from these TM X-ides are apt to exhibit higher OER activities than the corresponding, directly synthesized TM oxides/(oxy)hydroxides.[14,17,18,21] At present, further improvement of their OER activities and stabilities as well as elucidation of the primary origin of the resultant superior OER performance are becoming the focuses of research in this field.

Metallic nickel nitride (Ni_3N), on which we exclusively conducted experiments in this study, is a TM X-ide OER precatalyst. According to recent findings,[22–27] it was found that the Ni_3N electrode surface is transformed into layered nickel (oxy)hydroxide [$Ni(OH)_2$ and NiOOH] due to its self-oxidation during OER testing. This newly formed nickel (oxy)hydroxide surface is primarily responsible for catalyzing the OER. Incidentally, the contribution of surface oxide/(oxy)hydroxide species to the OER was also discussed in the reports of other TM pnictides (*e.g.*, CoN,[28] FeP,[29] CoP,[30,31] Ni_2P,[32–34] Ni_5P_4,[35] NiAs,[36] *etc.*). Recently, Trotochaud *et al.* reported that the incidental incorporation of trace Fe impurities from KOH electrolyte can increase the electrical conductivity and change the electronic structure of NiOOH, resulting in a dramatic increase in the OER activity of $Ni(OH)_2$/NiOOH.[37] According to several reports regarding (Ni,Fe)OOH,[38–41] the Fe concentration in NiOOH for obtaining the maximum OER activity has been reported to range from 12–25%. Furthermore, pure NiOOH has also been revealed to be a poor electrocatalyst for the OER.[37] Hence, in the Ni_3N precatalyst, there is a possibility that trace Fe also plays a critical role in boosting the OER activity of the nickel (oxy)hydroxide formed during the OER.

However, until now, little attention has been paid to studying how trace Fe incorporation impacts the OER activity of the Ni_3N precatalyst to understand the real active species for the OER. This is because almost all the reported Ni_3N-based electrocatalysts have been tested in unpurified KOH electrolyte that contains trace quantities of Fe.[23–27,42–56] As one example, Shalom *et al.* prepared the $Ni_3N/Ni(OH)_2$ electrocatalysts and tested them for the OER in both commercial and Fe-free 1 M KOH aqueous solutions.[22] As the $Ni_3N/Ni(OH)_2$ electrocatalysts demonstrated almost the same OER activities, they concluded that the influence of Fe impurities on the OER activity of their samples was minor. However, prior to the OER activity tests, their Ni_3N samples were oxidized to form $Ni(OH)_2$ *via* 500 cyclic voltammetry (CV) cycles in Fe-unpurified 0.1 M KOH. Accordingly, it is unknown if there was incorporation of trace quantities of Fe into the $Ni_3N/Ni(OH)_2$ samples during this CV oxidation process.

In this study, we prepared a Ni_3N precatalyst layer on nickel foam (Ni_3N/Ni foam) through room-temperature chemical oxidation and subsequent nitridation and investigated its transformation (self-oxidation) under the OER process in Fe-purified alkaline media (referred to here as "purified 1 M KOH"). Analytical techniques including X-ray diffraction, energy-dispersive X-ray spectroscopy, scanning electron microscopy, and X-ray photoelectron spectroscopy were employed to check the compositional and morphological changes of Ni_3N before and after OER CV testing. The electrochemical changes to the Ni_3N with OER CV testing were tracked using voltammetric techniques. Furthermore, to check the impact of Fe impurity incorporation on measured OER activities, the Ni_3N/Ni foam electrodes were tested for the OER in Fe-unpurified alkaline media ("unpurified 1 M KOH") as well. To more deliberately and evenly introduce trace Fe into the self-oxidized Ni_3N/Ni foam[57,58] and evaluate the OER activity in a condition close to practical conditions, a flow cell was used. Specifically, we conducted long-term OER chronopotentiometric (CP) tests to examine the relationship between the electrochemical changes and Fe incorporation over time. Importantly, the post-OER CV Ni_3N sample in purified 1 M KOH exhibited a higher OER overpotential (η) of 482 mV at a geometric current density of 20 mA cm_{geo}^{-2} compared to the post-OER CP Ni_3N sample (325 mV at 20 mA cm_{geo}^{-2}) as well as the previously reported Ni_3N/Ni foams (365 ± 24 mV at 20 mA cm_{geo}^{-2})[22,26,42,55] in unpurified 1 M KOH. Additionally, the OER CV test in purified 1 M KOH showed a decline in measured OER activities [η: 442.5 → 463.2 mV at 15 mA cm_{geo}^{-2}] whereas the OER CP test in unpurified 1 M KOH indicated an increase in measured OER activities [η: 315.7 → 293.3 mV at 15 mA cm_{geo}^{-2}]. These experimental findings evidently imply that the superior OER performance of the Ni_3N precatalyst in unpurified alkaline media mainly originates from the modified electronic properties of the self-oxidation-formed NiOOH due to the Fe incorporation.

Experimental

Materials

Nickel foam [>99.99%, porosity: ≥95% (80–110 pores per inch, average hole diameters about 0.25 mm), thickness: 1.6 mm, MTI Corporation], acetone (≥99.5%, Fisher Scientific), ethanol (Pharmco-Aaper), hydrochloric acid (Fisher Scientific), potassium peroxydisulfate (99.0%, BeanTown Chemical), potassium hydroxide (90%, Sigma Aldrich), and nickel(II) nitrate hexahydrate (99%, Acros Organics) were used as-received for synthetic and electrochemical experiments. Ultra-pure water (18 MΩ resistance) was used for all aqueous solutions. Notably, Fe-purified 1 M KOH aqueous solution was prepared by using a previously reported method [details are available in the ESI†],[37] to ignore the OER activity enhancement due to the incidental Fe incorporation during the electrochemical tests.

Ni_3N/Ni foam electrode preparation

Ni_3N/Ni foam was fabricated *via* the nitridation of the NiO/Ni foam precursor under a high-temperature NH_3 atmosphere. Prior to the fabrication, Ni foam was cleaned to remove impurities on the surface. Small and large Ni foam pieces [small: 30 × 10 mm (a part of the small Ni foam piece (*i.e.*, 20 × 10 mm) was pressed and compressed to minimize the capillary action during the electrochemical tests); large: 50 × 30 mm] were immersed in the following solutions (small: 5 mL per 1 piece; large: 300 mL per 12 pieces) while in an ultrasonic bath for 10 min each: (i) pure acetone, (ii) 3 M HCl aqueous solution, and (iii) deionized water. For performing the low-temperature chemical oxidation to synthesize NiO/Ni foams, one small and five large Ni foam pieces (all as-cleaned) were immediately immersed in 5 and 300 mL of 0.15 M

$K_2S_2O_8$ aqueous solutions, respectively, which is a previously reported procedure,[59] and kept for 12 h. Subsequently, the as-treated pieces were carefully rinsed with deionized water and dried at room temperature overnight.

For Ni_3N/NF synthesis, the as-prepared NiO/Ni samples were subjected to further oxidation in a box-type furnace at 350 °C for 2 h, with a heating ramp of 10 °C min^{-1}. Afterwards, the as-oxidized Ni foam pieces were placed onto a 101 × 67 × 3 mm quartz plate located in the center of a tube furnace and nitrided at 450 °C for 6 h at a heating ramp of 10 °C min^{-1} under an NH_3 flow (120 mL min^{-1}) and then cooled naturally to room temperature.

Characterization

X-ray diffraction (XRD) patterns of the samples were recorded using a Rigaku Miniflex 600 X-ray diffractometer (Rigaku, Japan) with Cu Kα radiation (λ = 1.54186 Å). The surface chemical compositions of the samples were investigated using an X-ray photoelectron spectrometer (XPS) model Axis-Ultra DLD (Kratos Analytical, USA) equipped with a monochromated 120 W Al $K\alpha_1$ X-ray source ($h\nu$ = 1486.5 eV). The binding energies of the elements of interest were corrected using the C 1s major peak of adventitious carbon at 284.8 eV. Casa XPS software was used for peak analysis. The sample morphologies were observed by a Quanta 650 environmental scanning electron microscope (ESEM, FEI, USA) with an energy dispersive X-ray spectroscopy (EDX) detector (XFlash 6|10, Bruker Nano GmbH, Germany). The Fe concentration of the unpurified 1 M KOH electrolyte with an internal standard (Y, 5 ppm) was estimated using a S2 PICOFOX total reflection X-ray fluorescence (TXRF) spectrometer (Bruker Nano GmbH, Germany) (Mo K radiation).

Electrochemical measurements

To evaluate OER performance, electrochemical measurements were conducted in purified 1 M KOH aqueous solution (pH ∼ 14) using a CHI601D electrochemical analyzer (CH Instrument, USA) with a standard three-electrode system consisting of the as-prepared small Ni_3N/Ni or Ni foam working electrode (area: 1 cm^2), a platinum plate counter electrode (area: 1 cm^2), and a Hg/HgO (1 M KOH) reference electrode at room temperature (see Fig. S1, ESI†). Multiple cyclic voltammetry (CV) scans were performed to examine the transformation of the Ni_3N/Ni and Ni foams. All the measurements were compensated by an 85% *iR*-drop.

To investigate the electrode surface area change during the long-term OER CV test, electrochemically active surface areas (ECSAs) were estimated from the electrochemical double-layer capacitances (C_{dl}s). Cyclic voltammograms (CVs) with different scan rates were obtained in the non-faradaic potential window (−0.2 to −0.1 $V_{Hg/HgO}$) to calculate C_{dl} from the scan-rate dependence of double-layer charging [$\Delta j/2 = (j_a - j_c)/2$].[60] The potentials applied relative to Hg/HgO were converted into the reversible hydrogen electrode (RHE) scale *via* the Nernst equation $\left[E_{RHE} = E_{Hg/HgO} + 0.0591 \times pH + E^{\circ}_{Hg/HgO}; E^{\circ}_{Hg/HgO}(1\ M\ KOH) = \sim 0.114\ V \text{ at } 25\ ^{\circ}C\right]$. Here, $E^{\circ}_{Hg/HgO}$ was determined by using the saturated calomel electrode (SCE, saturated KCl aqueous solution, 0.241 V *versus* standard hydrogen electrode).

Computational methods

Spin-polarized density functional theory (DFT) calculations in this study were carried out with the Vienna *ab initio* simulation package (VASP).[61,62] Core and valence electrons were respectively described by the projector augmented-wave method[63] and the Kohn–Sham wave functions expanded in a plane wave basis,[64] with a kinetic energy cutoff set as 400 eV. The electronic exchange and correlation were described by a generalized gradient approximation method with the functional developed by Perdew, Burke, and Ernzerhof.[65] The Brillouin zone was sampled using a (3 × 3 × 1) *k*-point mesh with the method developed by Monkhorst and Pack.[66] Structures were considered optimized after the forces of all atoms fell below 0.05 eV $Å^{-1}$. Based on the fact that Ni_3N is a Ni-rich material and the N-terminated surfaces are highly hydrophobic, only the Ni-terminated Ni_3N surfaces and Ni(111) were considered in our calculations.

Results and discussion

Ni_3N/Ni foam electrodes were fabricated through a two-step approach. First, NiO/Ni foam precursors were prepared *via* a low-temperature-oxidation method.[59] Subsequently, the as-prepared NiO/Ni foam precursors were nitrided at a high temperature (450 °C) under a constant NH_3 gas flow, resulting in Ni_3N/Ni foam. The resultant Ni_3N/Ni foam electrode was subjected to long-term OER cyclic voltammetric (CV) testing (potential range: 0.25 to 0.75 $V_{Hg/HgO}$, scan rate: 50 mV s^{-1}, cycle number: 1000) to investigate its transformation [electrochemical oxidation (self-oxidation)] to nickel oxide/(oxy)hydroxide in purified 1 M KOH aqueous solution. To elucidate the compositional and morphological transformation of Ni_3N during the long-term OER CV test, the pre- and post-OER Ni_3N/Ni foams were thoroughly characterized. Furthermore, to uniformly incorporate Fe into the self-oxidized Ni_3N/Ni foam[57,58] and check the impact of Fe incorporation on its OER performance under more practical conditions,[67] the Ni_3N/Ni foam was used in a flow cell with reagent grade (unpurified) KOH aqueous electrolyte.[68] Additionally, just as with the Ni_3N/Ni foam, pristine Ni foams were also investigated to check the difference between Ni_3N and Ni in the electrochemistry. In this Section, we discuss the results in the following order: (i) pre- and post-OER characterization, (ii) long-term OER CV tests in purified 1 M KOH aqueous solution, and (iii) flow cell tests in reagent grade 1 M KOH aqueous solution.

Characterization of pre- and post-OER Ni_3N/Ni foam

The unmagnified and magnified XRD patterns of the as-prepared nickel nitride/nickel foam are shown in Fig. 1a and b. The diffraction peaks can be assigned to hexagonal Ni_3N (ICDD PDF #70-9599) and cubic Ni (ICDD PDF #04-0850) without any diffraction peaks corresponding to impurity phases. Incidentally, the corresponding crystal structures of hexagonal Ni_3N and

cubic Ni are available in Fig. S2 (ESI†). After the long-term OER CV testing, the Ni_3N and Ni crystal structures were maintained (Fig. 1c and d). Moreover, the formation of new crystalline phases (*e.g.*, self-oxidized species) was not observed. As seen in Fig. S3 (ESI†), similar XRD results were also observed in the pre- and post-OER Ni foams. According to previous reports,[22,23,25,26] both Ni_3N and Ni should undergo self-oxidation under oxidizing potentials. Thus, there is a possibility that on the post-OER Ni_3N and Ni surfaces, amorphous oxide counterparts [*i.e.*, nickel (oxy)hydroxide] might be generated.

Thus, to ascertain the presence of amorphous self-oxidized species on the post-OER Ni_3N and Ni surfaces, EDX elemental mapping analyses were conducted on the pre- and post-OER samples. In the as-prepared Ni_3N/Ni foam, Ni (green) and N (blue) elements were homogeneously distributed (Fig. 2a). Weak O (red) signals were also confirmed, which may correspond to the partial oxidation of the as-prepared sample surface due to exposure to ambient air. After the long-term OER CV test (Fig. 2b), Ni and N signals remained, while the O signal intensity increased. In the case of the pristine Ni foam, O signals were not observed (Fig. S4a, ESI†). However, relatively weak, evenly distributed O signals appeared after the OER test (Fig. S4b, ESI†). As just described, for both the Ni_3N/Ni and Ni foams, O incorporation proceeded after the OER testing (Table S1, ESI†). In particular, the O/Ni atomic ratio of the Ni_3N/Ni foam drastically increased from 0.016 to 0.320 following the OER test. Considering these facts, amorphous nickel (oxy)hydroxide layers might form on the post-OER Ni_3N and Ni surfaces. More interestingly, the post-OER Ni_3N/Ni showed a much higher O/Ni atomic ratio (0.320) than the post-OER Ni (0.013), which implies that Ni may be more resistant to oxidation than Ni_3N. This point will be discussed in greater detail later in the paper.

To inspect the morphologies of the Ni_3N/Ni and Ni foams before and after the long-term OER CV tests, SEM measurements were performed (Fig. 3 and Fig. S5, S6, ESI†). The low- and high-resolution SEM images of the as-prepared Ni_3N/Ni foam are shown in Fig. S5a (ESI†) and Fig. 3a. Compared with the pristine Ni foam (Fig. S6a, ESI†), the as-prepared Ni_3N/Ni foam surface is rougher. This roughness was likely due to (i) the amorphous NiO nanocluster growth on the Ni foam surface through low-temperature oxidation

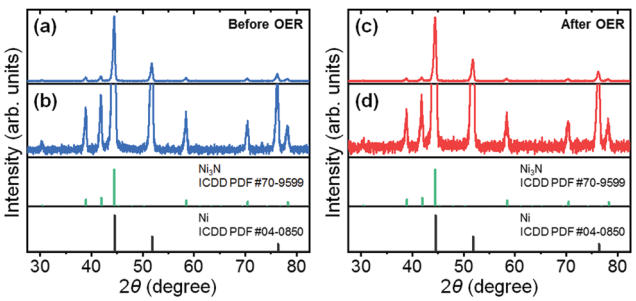

Fig. 1 Unmagnified and magnified XRD patterns of Ni_3N/Ni foam electrode (a and b) before and (c and d) after 1000 cycles of the OER CV (0.25 to 0.75 $V_{Hg/HgO}$) at a scan rate of 50 mV s^{-1} in purified 1 M KOH aqueous electrolyte. Notably, the diffraction patterns were recorded for the same sample before and after the OER CV test.

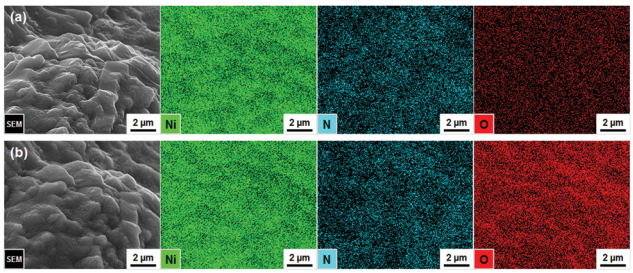

Fig. 2 SEM and EDX elemental mapping images (accelerating voltage: 30 kV) of Ni_3N/Ni foam electrode (a) before and (b) after 1000 cycles of the OER CV (0.25 to 0.75 $V_{Hg/HgO}$) at a scan rate of 50 mV s^{-1} in purified 1 M KOH aqueous electrolyte. Notably, the images were taken at the same position before and after the OER CV test.

(Ni → NiO)[59] and (ii) the subsequent lattice contraction that accompanies the replacement of O with N in the amorphous NiO precursor during the nitridation (NiO → Ni_3N).[69] After the OER test, the self-oxidized Ni_3N/Ni foam macroscopically maintained the surface morphology of the as-prepared Ni_3N/Ni foam (see Fig. S5, ESI†). However, from a microscopic view (Fig. 3), the relatively compact Ni_3N surface was transformed into a nano-porous surface (and more available for electrolyte penetration) of its oxide counterparts [$Ni(OH)_2$ and NiOOH][22,23,25,26] through the long-term OER process. By contrast, on the Ni foam, a compact layer (it doesn't appear to be nano-porous like the Ni_3N material) of its oxide counterparts formed after the OER test (Fig. S6b, ESI†). This morphological difference possibly resulted from the different extent of atomic packing of Ni in the hexagonal Ni_3N and cubic Ni crystal structures (Fig. S2, ESI†). Specifically, Ni_3N has a slightly longer Ni–Ni interatomic distance (d_{Ni-Ni} = 2.6 Å) than Ni (d_{Ni-Ni} = 2.5 Å). Accordingly, the highly porous structure of $Ni(OH)_2$ and NiOOH derived from Ni_3N can be realized due to the relatively rough surface and long Ni–Ni interatomic distance of Ni_3N.

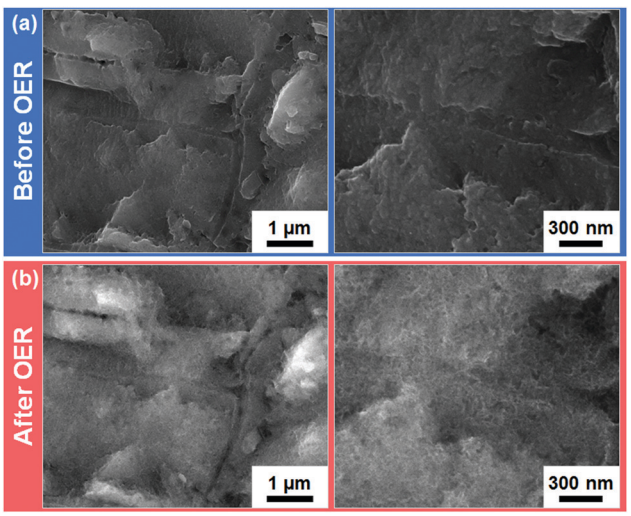

Fig. 3 High-resolution SEM images of Ni_3N/Ni foam electrode (a) before and (b) after 1000 cycles of the OER CV (0.25 to 0.75 $V_{Hg/HgO}$) at a scan rate of 50 mV s^{-1} in purified 1 M KOH aqueous electrolyte. Notably, the images were taken at the same position before and after the OER CV test.

To investigate the surface chemical composition and states of the Ni_3N/Ni and Ni foams before and after the long-term OER CV tests, XPS measurements were conducted. The Ni $2p_{3/2}$ and N 1s XPS spectra of the pre- and post-OER Ni_3N/Ni foams are shown in Fig. 4. In the pre- and post-OER Ni $2p_{3/2}$ spectra (Fig. 4a and b), the deconvoluted peaks can be assigned to five components: (i) Ni_3N (852.8 eV),[23,26] (ii) NiO (854.5 eV),[70] (iii) $Ni(OH)_2$ (855.3 eV),[70] (iv) NiOOH (855.8 eV),[70] and (v) satellites (around 860.6 eV),[26,71] respectively. The Ni $2p_{3/2}$ peaks of NiO and $Ni(OH)_2$ in the as-prepared Ni_3N/Ni foam imply that the product surface might be partially oxidized by ambient air exposure. After the OER test, the Ni $2p_{3/2}$ peak of Ni_3N disappeared and NiOOH and $Ni(OH)_2$ formation was confirmed. These phenomena indicate that the surface oxidation of Ni_3N into NiOOH and $Ni(OH)_2$, which agrees with previous reports.[22,23,25,26] As for the Ni foam, similar surface oxidation was observed after the OER test. The XPS measurement results of the pre- and post-OER Ni foams are also available in Fig. S7 (ESI†). The N 1s spectrum of the as-prepared Ni_3N/Ni foam was deconvoluted into two components (Fig. 4c). The high intensity peak at 398.3 eV is assignable to the lattice nitrogen species in Ni_3N.[22] The other peak is likely associated with surface-adsorbed NH_x (400.0 eV).[72] After the OER test, the N 1s signal almost disappeared, suggesting that the nitrogen species do not directly contribute to the OER process. From the above XRD, EDX, and XPS results (Fig. 1, 2, and 4), we conclude that a Ni_3N@$Ni(OH)_2$/NiOOH core@shell structure formed after the OER test. To further support this conclusion, Fig. S8 (ESI†) shows the electrochemical stability map (Pourbaix diagram and Gibbs free energy overlay) of Ni_3N as theoretical evidence. Ni_3N is unstable across a wide range of pH value and potentials. Thus, it is easily expected that the Ni_3N surface, which is in contact with the electrolyte, can be oxidized under OER conditions and the Ni_3N-derived nickel (oxy)hydroxide may act as the OER active sites rather than the initial Ni_3N.

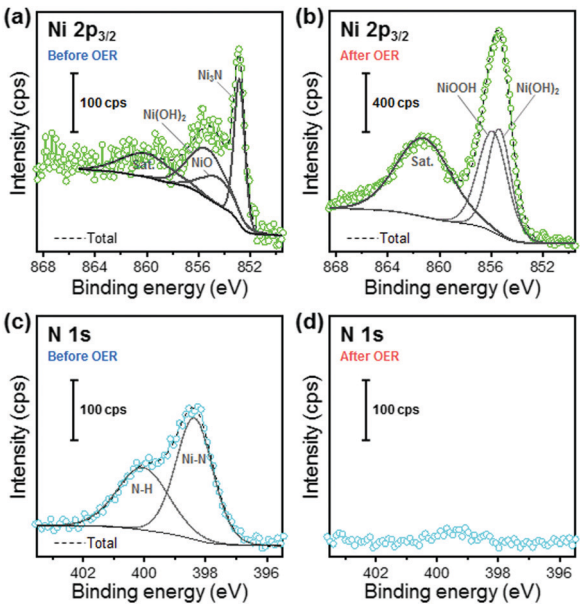

Fig. 4 Ni $2p_{3/2}$ and N 1s XPS core-level spectra of Ni_3N/Ni foam electrode (a and c) before and (b and d) after 1000 cycles of the OER CV (0.25 to 0.75 $V_{Hg/HgO}$) at a scan rate of 50 mV s^{-1} in purified 1 M KOH aqueous electrolyte.

Electrochemical behavior of Ni_3N/Ni foam anode in purified KOH electrolyte

The OER performance of the Ni_3N/Ni foam electrode was studied through voltammetric measurements using a conventional three-electrode system (see Fig. S1, ESI†). Here, purified 1 M KOH aqueous solution was used as an electrolyte to prevent incidental Fe incorporation. Additionally, to check the effect of the substrate material on the electrochemical results, a Ni foam electrode was tested as well. We first performed continuous OER CV scans between 0.25 to 0.75 $V_{Hg/HgO}$ for 1000 cycles at a scan rate of 50 mV s^{-1} on the Ni_3N/Ni and Ni foam electrodes. Periodically, changes in the OER overpotential (η at a current density of 15 mA cm_{geo}^{-2}) and CV-derived C_{dl} were measured and reported as a function of CV cycle number (Fig. 5 and Fig. S9–S12, ESI†). Here, the CV-derived C_{dl} values were used to estimate the ECSAs of the Ni_3N/Ni and Ni foams. Furthermore, the anodic and cathodic peaks, which are mainly attributed to the oxidation and reduction of Ni species [*i.e.*, γ-NiOOH, β-NiOOH, NiO_2, α-$Ni(OH)_2$, and β-$Ni(OH)_2$],[37,73,74] were confirmed, which agree with the XPS results, and monitored over the CV cycling (Fig. S9, S11, and S13, ESI†). Importantly, the intensities of these anodic peaks may correspond to the thickness/quantity of nickel oxide/(oxy)hydroxide shells formed due to the

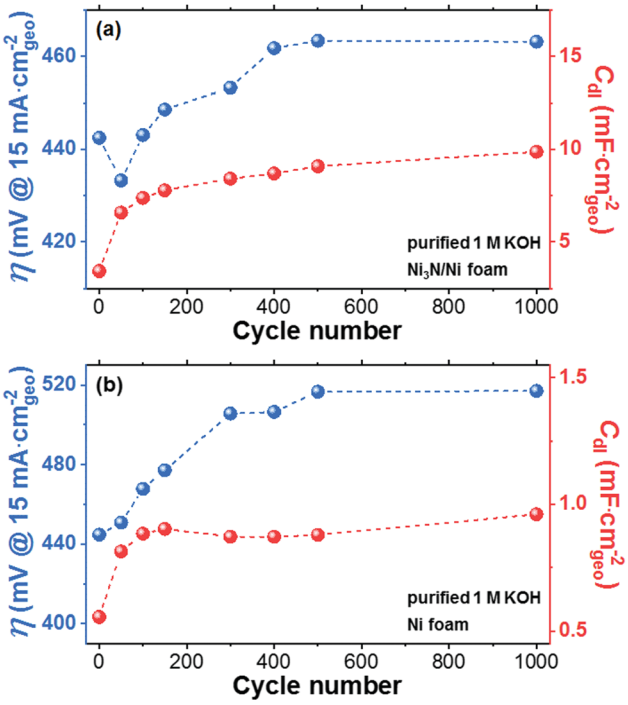

Fig. 5 Trend of OER overpotential (blue) and double layer capacitance (red) *vs.* cycle number of CV for Ni_3N/Ni and Ni foam electrodes. Multi-CV tests were performed in the potential range of 0.25 to 0.75 $V_{Hg/HgO}$ with the scan rate of 50 mV s^{-1} for 1000 cycles in purified 1 M KOH aqueous electrolyte.

self-oxidation of Ni_3N and Ni during the OER.[36] Herein, the OER activity trend during the CV test can be explained by two main parameters: (i) the CV-derived C_{dl} value and (ii) the peak intensities for the oxidation of Ni species. In the case of the Ni_3N/Ni foam (Fig. 5a), the rapid increase of the CV-derived C_{dl} value observed (63 μF mA cm_{geo}^{-2} $cycle^{-1}$) during the first 50 cycles was due to the self-oxidation of Ni_3N into layered nickel (oxy)hydroxide,[75] which may have resulted in an increase in the number of OER active sites and thus an increase in OER activity.[14] Afterword, in accordance with increasing the CV cycle number, the increase of the CV-derived C_{dl} value became gentler and the CV-derived C_{dl} values almost leveled off from 500 to 1000 cycles. However, in contradiction to our earlier explanation, a continuous decline in the OER activity was observed from 50 to 500 cycles. After 500 cycles, the OER activity became steady. Interestingly, the Ni oxidation peaks are greatly amplified throughout the course of the CV test (see Fig. S9a–h, ESI†), suggesting an increase of the thickness/quantity of the nickel oxide/(oxy)hydroxide shell over Ni_3N. As shown in Fig. S13a (ESI†), the post-OER Ni_3N/Ni foam exhibited the formation of NiOOH (*i.e.*, γ-NiOOH and β-NiOOH) as a main phase. Also, it is known that Ni_3N is a metallic conductor whereas NiOOH is a semiconductor [incidentally, $Ni(OH)_2$ is an insulator].[23,37,44] Accordingly, the OER activity decline (50–500 cycles) was probably caused by a decrease in electrical conductivity due to the growth of the nickel oxide/(oxy)hydroxide shell. On the other hand, in the case of the Ni foam (Fig. 5b), the CV-derived C_{dl} value sharply increased in the early stage (0–50 cycles) without a concurrent increase in OER activity. Since the degree of increase in the CV-derived C_{dl} for Ni (5.2 μF cm_{geo}^{-2} $cycle^{-1}$) is much smaller than that for Ni_3N (63 μF cm_{geo}^{-2} $cycle^{-1}$), the OER activity-enhancing effect derived from the ECSA increase may be overwhelmed by the OER activity-declining effect from the electrical conductivity decrease owing to the growth of a nickel oxide/(oxy)hydroxide shell over the Ni metal (Fig. S11a and b, ESI†). Thereafter, the Ni foam electrode exhibited an electrochemical behavior (in OER activity, ECSA, and self-oxidation) similar to the Ni_3N/Ni foam (50–1000 cycles).

Similarly to the CV-derived value for C_{dl}, the surface redox reaction of transition metal ions at transition metal (oxy)hydroxides (*e.g.*, $Ni_{0.8}Fe_{0.2}O_xH_y$) can conventionally be a descriptor to estimate the number of active sites.[76,77] Specifically, the redox active Ni species can be quantified as OER active sites using the integration of the main oxidation peaks of Ni^{2+}/Ni^{3+} (A_1 and A_2 in Fig. S13, ESI†). However, in both the Ni_3N/Ni and Ni foams, even though the CV-derived C_{dl} value changes (Fig. 5 and Fig. S10, S12, ESI†) it did not follow the changes in the Ni^{2+}/Ni^{3+} oxidation peak intensities (Fig. S9a–h and S11a–h, ESI†). Importantly, despite the continuous increase in intensity of the Ni^{2+}/Ni^{3+} oxidation peaks during CV cycling, the CV-derived C_{dl} values stabilized from 50 to 1000 cycles. Here, since the Ni^{2+}/Ni^{3+} oxidation peak intensity may correlate with the amount of NiOOH species formed by the self-oxidation of Ni_3N or Ni, we conclude that the amount of surface NiOOH species continuously increased over the CV cycling.[36] Given that this does not correlate with an increase in OER performance, it instead implies that not all NiOOH species on the Ni_3N and Ni surfaces can participate in the OER. It is well-known that both $Ni(OH)_2$ and NiOOH possess layered structures and that the surface Ni^{2+}/Ni^{3+} redox reactions involve changes in crystal structure [*i.e.*, $Ni(OH)_2 \leftrightarrow$ NiOOH].[75] According to recent studies about transition metal (oxy)hydroxide nanosheets,[78,79] single-layered $Ni(OH)_2$ nanosheets were transformed into nanoparticles during electrochemical Ni redox cycling. This shape transformation likely occurs because of (i) cracking from mechanical stress [*e.g.*, Ni–Ni interatomic distance changes (d_{Ni-Ni} = 3.12 Å for $Ni(OH)_2 \leftrightarrow d_{Ni-Ni}$ = 2.86 Å for NiOOH)][80] and (ii) the ripening phenomena.[79] Presumably, in our experiments, a similar cracking and ripening occurred as the Ni_3N and Ni metal-derived nickel (oxy)hydroxide shells were amorphized during CV cycling. Furthermore, as shown in Fig. S14 (ESI†), the contraction of nickel (oxy)hydroxide shells could have proceeded, resulting in the formation of an underlying layer of compact nickel (oxy)hydroxide. Note that such a compact nickel (oxy)hydroxides may possess a "cornflake-in-milk"-like structure [cornflake: NiO_xH_y nanoflake; milk: electrolyte (see Fig. S14, ESI†)] and be able to participate in reversible Ni redox reactions but not the OER. Accordingly, only the outermost surface nickel (oxy)hydroxides may be able to contribute to the OER process. This may explain the observed mismatch between the trends of the CV-derived C_{dl} values and the Ni^{2+}/Ni^{3+} oxidation peak intensities.

After 1000 cycles, the Ni_3N/Ni foam recorded a lower OER overpotential of 482 mV at 20 cm_{geo}^{-2} than the Ni foam (534 mV). This is mainly because Ni_3N-derived nickel (oxy)hydroxide exhibited a unique nano-porous structure (see Fig. 3b) with an ECSA (~246.8 cm^2) approximately 10 times higher than that of Ni metal-derived nickel (oxy)hydroxide (~24.02 cm^2). Notably, in comparison to the previously reported Ni_3N/Ni foams in unpurified electrolytes, our post-OER Ni_3N/Ni foam in the purified electrolyte showed worse OER activity, despite having a higher CV-derived C_{dl} values (see Table S2, ESI†).[22,26,42,55] The high OER overpotential can be attributed to the poor OER activity of pure NiOOH derived from Ni_3N in purified electrolyte.[37] The incidental incorporation of Fe impurities from unpurified electrolytes can increase the NiOOH conductivity and modify the NiOOH electronic structure, resulting in OER activity enhancement.[37,39,81] As almost all the reported Ni_3N/Ni foams were tested in unpurified electrolytes, Fe impurities were likely incorporated into the Ni_3N-derived nickel (oxy)hydroxide electrocatalysts, resulting in the relatively low OER overpotentials (365 ± 24 mV at 20 mA cm_{geo}^{-2}).[22,26,42,55] Conversely, we used a purified electrolyte which prevented Fe incorporation and thus our Ni_3N-derived nickel (oxy)hydroxides behaved electrochemically like a pure nickel (oxy)hydroxide with poor OER performance (see Fig. S13 and corresponding descriptions in the ESI†). Notably, contrary to previous findings in which samples are tested in purified KOH but pre-oxidized in unpurified KOH,[22] our results and those of previous reports show that incorporation of trace Fe from the KOH electrolytes is essential if a Ni_3N OER precatalyst is to achieve notable OER activity (more details are available in the descriptions below Fig. S13 in the ESI†).

To examine the intrinsic OER activity of the Ni_3N/Ni and Ni foams after 1000 cycles, the current densities of each calculated using the ECSA at the overpotential of 450 mV are demonstrated

in Fig. S15 (ESI†). From the XPS results (Fig. 4 and Fig. S7, ESI†), both the post-OER Ni_3N/Ni and Ni foams possess similar $Ni(OH)_2$/NiOOH surfaces, and thus one would expect that both the samples might show the same intrinsic OER activity. We find, however, that the Ni foam exhibited a higher intrinsic OER activity (-0.21 mA cm_{ECSA}^{-2}) than the Ni_3N/Ni foam (-0.05 mA cm_{ECSA}^{-2}) (Fig. S15, ESI†). This intrinsic OER activity difference can be accounted for by the difference in the total electrode conductivity. As displayed in Fig. S13 (ESI†), the Ni oxidation peak intensities of the Ni_3N sample were much larger than those of the Ni metal sample, indicating a larger yield of nickel oxide/(oxy)hydroxide for the Ni_3N sample. In addition, the O/Ni atomic ratio of the post-OER Ni_3N/Ni foam (0.320) was much higher than that of the post-OER Ni foam (0.013) (see Table S1, ESI†). Therefore, after the long-term OER CV tests, the as-formed nickel oxide/(oxy)hydroxide shell over Ni_3N was probably thicker than the shell over the Ni metal, or at least the amount of the as-formed nickel oxide/(oxy)hydroxide over Ni_3N may be greater than that of the as-formed nickel oxide/(oxy)hydroxide over Ni (see Fig. S14, ESI†). This thick oxide/(oxy)hydroxide shell over Ni_3N may reduce hole access at surface-electroactive sites (reducing the electrical conductivity), thus lowering the intrinsic OER activity. Based on these results, we can also predict that compared to Ni metal, Ni_3N may experience a higher extent of self-oxidation during the OER process.

Next, we performed density functional theory (DFT) calculations for the reaction on Ni_3N and pure Ni metal surfaces. Specifically, $Ni_3N(100)$, $Ni_3N(110)$, and Ni(111) were analyzed with the computational hydrogen electrode (CHE) method with the OER mechanism proposed by Man *et al.* (Fig. 6).[82] Herein, using the DFT results, we attempted to explain the oxidation resistances of Ni_3N and Ni metal rather than their intrinsic OER activities. As demonstrated in Fig. 6a, since the first steps are exothermic, $Ni_3N(100)$ and (110) can easily be covered with HO* and O*. Compared to the first and second steps (*i.e.*, formation of HO* and O*), HOO* formation on $Ni_3N(100)$ and (110) is much more endothermic, resulting in partial oxidation of Ni_3N to Ni–O/Ni–OH during the OER. In the case of Ni(111), as HOO* formation is much more endothermic than the formation of HO* and O*, partial oxidation of Ni metal to Ni–O/Ni–OH may also occur. However, Ni(111) may experience slight difficulty in the formation of HO* and O* as the first step is more endothermic compared to that of Ni_3N. This is due in part to the lower coordination number of Ni-sites on Ni_3N structures compared to that on close-packed pure Ni metal surface, resulting in stronger binding energies to these oxygen-containing species. Consequently, Ni_3N may have a lower oxidation resistance than Ni metal, in agreement with our experimental observations.

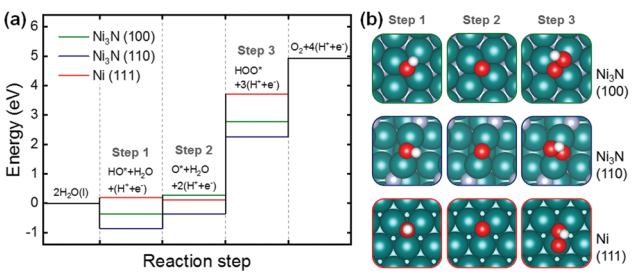

Fig. 6 (a) Calculated OER free energy diagram on $Ni_3N(100)$, $Ni_3N(110)$, and Ni(111) under the potential of 0 V. (b) Optimized configurations of OER adsorbate on $Ni_3N(100)$, $Ni_3N(110)$, and Ni(111). Green, grey, red, and white spheres represent Ni, N, O, and H atoms, respectively.

Electrochemical behavior of Ni_3N/Ni foam anode in reagent grade KOH electrolyte

To investigate the effect of Fe impurities on OER performance, the Ni_3N/Ni and Ni foam electrodes were tested in reagent grade 1 M KOH aqueous electrolyte. According to the TXRF result, the Fe concentration of our reagent grade 1 M KOH aqueous electrolyte was ~ 1.15 mg L^{-1}. To ensure the uniform uptake of Fe impurities on our sample electrodes[57,58] and evaluate their OER performances in a condition close to practice,[67] we used a flow cell system (Fig. S16, ESI†),[68] about which more details are available in the ESI.† As shown in Fig. 7, we performed 20 h chronopotentiometry (CP) runs for the Ni_3N/Ni and Ni foam electrodes at a current density of 10 mA cm_{geo}^{-2}. To track changes in (1) the OER overpotential (η at a current density of 15 mA cm_{geo}^{-2}), (2) the Ni^{2+}/Ni^{3+} oxidation peak, and (3) the CV-derived C_{dl} with electrode surface self-oxidation and Fe impurity incorporation, the CP tests were stopped every 4 h (*i.e.*, 0, 4, 8, 12, 16, and 20 h) to record linear sweep voltammograms (LSVs) and CVs. Note that the post-OER CP XRD and XPS analyses revealed complete transformations of Ni_3N/Ni and Ni foam surfaces into $Ni(OH)_2$/NiOOH (see Fig. S17–S19, ESI†), similar to that observed for the post-OER CV Ni_3N/Ni and Ni foam surfaces in purified 1 M KOH aqueous electrolyte.

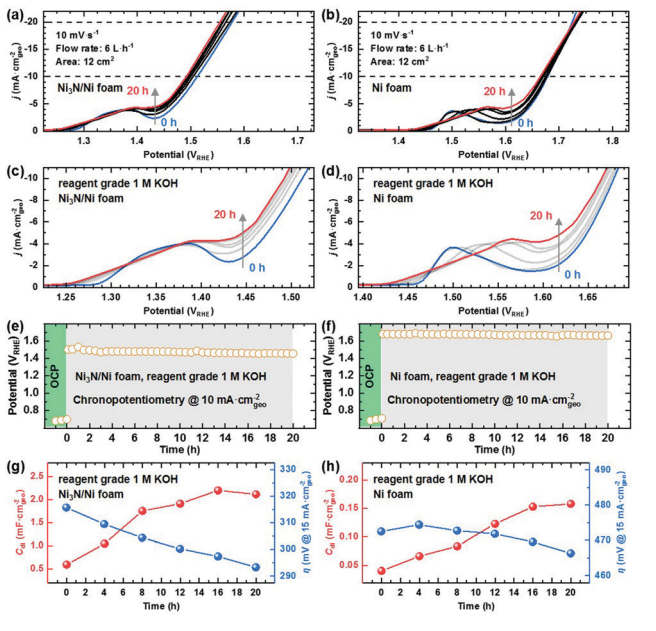

Fig. 7 Electrochemical testing results of Ni_3N/Ni and Ni foams in reagent grade 1 M KOH aqueous electrolyte: (a and b) unmagnified and (c and d) magnified anodic LSVs obtained at intervals of 4 h during 20 h CP tests (at 10 mA cm_{geo}^{-2}), (e and f) 20 h CP plots, and (g and h) trend of OER overpotential (blue) and double layer capacitance (red) *vs.* time.

Moreover, the presence of Fe in the newly-formed $Ni(OH)_2$/NiOOH layers on Ni_3N/Ni and Ni foams was also confirmed by XPS (Fig. S20, ESI†).

First, we seek to explain the OER CP self-oxidation behaviors of Ni_3N and Ni metal by using the Ni^{2+}/Ni^{3+} oxidation peaks of the samples (Fig. 7a–d). After the 20 h CP tests, the Ni^{2+}/Ni^{3+} oxidation peaks of both the Ni_3N/Ni and Ni foams were more or less the same intensity (Fig. 7c and d), implying that the self-oxidation degree of Ni_3N might be nearly equal to that of Ni metal (Fig. S21, ESI†). These similar degrees of self-oxidation are mainly due to the different applied potentials during the OER CP tests. Specifically, the Ni_3N/Ni foam showed a lower applied potential ($\sim$1.47 V_{RHE}) than the Ni foam ($\sim$1.67 V_{RHE}) at a constant current density of 10 mA cm_{geo}^{-2}, which may enable similar degrees of self-oxidation for Ni_3N and Ni metal. More interestingly, both the Ni_3N/Ni and Ni foams experienced slight increases in the intensity of the Ni^{2+}/Ni^{3+} oxidation peaks during the long-term OER tests. However, the degree of increase observed in the Ni oxidation peaks during the OER CP tests is much smaller compared with those in the OER CV tests. These suppressions of the Ni oxidation peak intensity increases for the OER CP tests can be explained by the following two reasons: (i) reduction of structural damage in the OER process by the use of the CP technique and (ii) enhancement of electrical conductivity due to the Fe impurity incorporation. As described earlier, the CV-driven OER test involves the crystal structural changes [*i.e.*, $Ni(OH)_2 \leftrightarrow$ NiOOH] of the self-oxidized Ni_3N and Ni surfaces caused by the anodic and cathodic sweeps, which leads to crack formation.[79] The as-formed cracks likely allow the electrolyte to penetrate the self-oxidation-derived passivation layer all the way to the un-oxidized initial material (*i.e.*, Ni_3N, Ni metal) and induce its further self-oxidation. In contrast, the CP-driven OER test does not require the surface Ni^{2+}/Ni^{3+} redox reactions because of the roughly constant applied potentials. Thereby, the CP technique can restrain the crystal structural damage, electrolyte penetration, as well as self-oxidation. Fig. S22 shows the SEM images of the post-OER CP Ni_3N/Ni and Ni foam surfaces. Especially for the Ni_3N/Ni foam, the post-OER CP sample (Fig. S22a, ESI†) seemingly has a lower porosity than the post-OER CV sample (Fig. 3b), which represents evidence for the restrained structural damage. Furthermore, the self-oxidation of the precatalyst (*i.e.*, Ni_3N, Ni metal) during the OER may generally occur due to holes accumulated by the applied bias near the electrode surface. Thus, by increasing the electrical conductivity of the electrode surface, the holes can be utilized effectively for the OER and the self-oxidation may be suppressed. According to the study reported by Trotochaud *et al.*,[37] Fe incorporation can increase NiOOH conductivity 30–60-fold (with 5–25% Fe), which may also lower the degree of self-oxidation. Incidentally, Trotochaud *et al.* also found that a NiOOH sample tested in unpurified KOH electrolyte possesses $\sigma \approx 2.5$ mS cm^{-1}, whereas a NiOOH sample under Fe-free conditions has values for $\sigma \approx 0.1$ to 0.2 mS cm^{-1}.[37]

To gain a better understanding of the OER activity transition during the OER CP testing, Fig. 7g and h show the OER overpotentials and CV-derived C_{dl} values as a function of time for the Ni_3N/Ni and Ni foam electrodes. Unlike the findings in the purified electrolyte, both samples exhibited continuous reductions in the OER overpotential in the unpurified electrolyte. This OER activity enhancement is probably achieved by the continuous increases in intrinsic OER activity and ECSA owing to gradual Fe impurity incorporation and layered nickel (oxy)-hydroxide formation, respectively.

To more deeply probe the intrinsic OER activity for each sample, we calculated the ECSA-based current densities at the overpotential of 450 mV. As seen in Fig. S15 and S23 (ESI†), the Ni_3N/Ni and Ni foams in unpurified electrolyte reached much higher intrinsic OER activities (Ni_3N/Ni foam: -0.76 mA cm_{ECSA}^{-2}; Ni foam: -3.1 mA cm_{ECSA}^{-2}) compared with the foams in the purified electrolyte (Ni_3N/Ni foam: -0.05 mA cm_{ECSA}^{-2}; Ni foam: -0.21 mA cm_{ECSA}^{-2}). These OER activity improvements can be caused by the Fe impurities from unpurified electrolytes and enhanced mass transfer due to the use of the flow cell.[37,39,68] Curiously, although both samples have the same surface chemical compositions (see Fig. S19, ESI†) and similar amounts of self-oxidized species [$Ni(OH)_2$/NiOOH], the Ni foam demonstrated a higher intrinsic OER activity in comparison with the Ni_3N/Ni foam after the OER CP tests in the unpurified electrolyte. This difference in intrinsic OER activity might be because of the different Fe incorporation level per ECSA for each sample. Klaus *et al.* reported that the Fe incorporation level increases logarithmically with respect to aging time for which a $Ni(OH)_2$ electrode is immersed in unpurified 1 M KOH aqueous solution (in the absence of applied potential).[39] In this work, since we immersed the Ni_3N/Ni and Ni foams in unpurified electrolyte for almost same time (at least 20 h) during the OER CP tests, it is likely the total Fe uptake within both foams will be almost the same. However, because of the higher ECSA of the Ni_3N/Ni foam, the Ni foam probably reaches a higher Fe incorporation level per ECSA than the Ni_3N foam, resulting in the higher intrinsic OER activity of the Ni foam. To support this possibility, we show the magnified LSVs (Fig. 7c and d). In general, it is well-known that an anodic shift of the Ni^{2+}/Ni^{3+} oxidation peaks and an increase in OER activity happen with increasing the Fe incorporation level within nickel oxyhydroxide (or increasing x in $Ni_{1-x}Fe_xOOH$).[37,39,83–85] During the long-term OER CP tests in unpurified electrolyte, both the Ni_3N/Ni and Ni foams showed the Ni^{2+}/Ni^{3+} oxidation peak shifting and OER activity enhancement, which is evidence for the Fe uptake within our electrodes. However, compared with the Ni_3N/Ni foam, the Ni foam exhibited larger anodic shifts of the Ni^{2+}/Ni^{3+} oxidation peak during the OER test, indicating a higher x value in $Ni_{1-x}Fe_xOOH$ (or a higher Fe incorporation level per ECSA). For this reason, the Ni foam obtained a higher intrinsic OER activity than the Ni_3N/Ni foam after the OER CP testing. It is worth noting that $Ni_{1-x}Fe_xOOH$ species act as OER electroactive sites for the Ni_3N and Ni metal precatalysts in unpurified electrolyte.

Here, we also discuss a possible mechanism for Fe incorporation into the self-oxidized Ni_3N/Ni and Ni foam electrodes. According to a previous report,[38] initially, Fe impurity in unpurified electrolyte is incorporated at the edges/defects of the Ni_3N- and Ni-derived NiO_xH_y nanoflakes. Subsequently, the

Fe impurity is further incorporated into the bulk of the NiO_xH_y nanoflakes while Fe also remains at their edge/defect sites. Importantly, the Fe impurity is incorporated throughout the electrolyte-permeable regions of the Ni_3N/Ni and Ni foam electrodes (self-oxidized part: NiO_xH_y layer).[86]

Finally, we further discuss the geometric OER activity of the foam-type electrodes in unpurified electrolyte. After the long-term OER CP tests, the Ni_3N/Ni foam showed a higher geometric OER activity than the Ni foam despite its lower intrinsic OER activity (Table S2, ESI†). This higher geometric OER activity of the post-OER CP Ni_3N/Ni foam may result from its higher ECSA. Furthermore, as listed in Table S2 (ESI†), the geometric OER activity of our Ni_3N/Ni foam (in a flow cell) compares favorably with those of other reported foam-type Ni_3N samples (in a standard three-electrode cell). This may be the result of the improved mass transfer due to the use of a flow cell.[57,68] From the comparisons to literature values, the use of a flow cell is effective for further enhancing the geometric OER activity. This strategy can also be adapted to other foam-type electrocatalysts.

This study investigated Fe impurity incorporation effects on the OER activity of a Ni_3N precatalyst. It is noteworthy that geometric OER activity degradation was observed after the OER CV test in the purified electrolyte whereas the geometric OER activity continuously increased during the OER CP test in the unpurified electrolyte. These different behaviors are likely caused by the presence or absence of Fe impurities in the electrolyte. From our findings, we would expect other Ni-based OER precatalyst performances to also be affected for the better by Fe impurities from the electrolyte, for which further investigation is necessary in the future.

Conclusions

In summary, a Ni_3N precatalyst was successfully fabricated on nickel foam *via* low-temperature chemical oxidation and subsequent nitridation. Then, the as-prepared Ni_3N/Ni and as-purchased Ni foams were subjected to the OER CV and CP tests in purified and unpurified 1 M KOH aqueous electrolytes in standard three-electrode and flow cells, respectively. In both electrolytes, the partial self-oxidation of solid Ni_3N surfaces results in amorphous, nano-porous nickel oxide/(oxy)hydroxide layers. Meanwhile, Ni metal surfaces were partially self-oxidized into amorphous, compact nickel oxide/(oxy)hydroxide. Interestingly, our theoretical and experimental results indicate that Ni_3N has a lower oxidation resistance than Ni metal. In the purified electrolyte, the Ni_3N/Ni and Ni foams demonstrated decreases in measured geometric OER activities during continuous CV tests. This is mainly because of the relatively low electrical conductivity and OER activity of pure NiOOH. In contrast, when testing in unpurified electrolyte the geometric OER activities of the Ni_3N/Ni and Ni foams increased along with the NiOOH formation and continuous Fe impurity incorporation since trace Fe can improve the electronic properties of NiOOH. This Fe incorporation would also be expected to happen in other Ni-based OER precatalysts, which future works need to examine. In addition, regardless of whether trace Fe impurities exist, the Ni_3N/Ni foams exhibited lower OER overpotentials than the Ni foams due to the higher ECSAs of post-OER Ni_3N samples. Most notably, the post-OER CP Ni_3N/Ni foam in a flow cell achieved a significantly higher geometric OER activity (η: 262 mV at a current density of 10 mA cm_{geo}^{-2}) than previously reported foam-type Ni_3N electrocatalysts in unpurified electrolytes, which may result from the improved mass transfer. This flow cell strategy can also be applicable to any other electrodes with high surface areas, such as foam-type electrodes, and be useful for developing rational electrode design in more practical conditions.

Author contributions

K. Kawashima: conceptualization, investigation, formal analysis, writing-original draft, R. A. Márquez-Montes: investigation, formal analysis, writing-original draft, H. Li: investigation, formal analysis, writing-review and editing, K. Shin: investigation, formal analysis, writing-review and editing, C. L. Cao: investigation, writing-review and editing, K. M. Vo: investigation, writing-review and editing, Y. J. Son: investigation, writing-review and editing, B. R. Wygant: investigation, writing-review and editing, A. Chunangad, investigation, writing-review and editing, D. H. Youn: funding acquisition, writing-review and editing, G. Henkelman: resources, funding acquisition, writing-review and editing, V. H. Ramos-Sáncheze: resources, writing-review and editing, C. B. Mullins: conceptualization, supervision, resources, funding acquisition, writing-original draft.

Conflicts of interest

The authors declare no competing financial interest.

Acknowledgements

The authors gratefully acknowledge the support of the National Science Foundation (NSF) *via* Grant CHE-1664941 (C. B. M.) for the experimental portion of the paper and the U.S. Department of Energy (DOE) *via* Grant DE-SC0010576 (G. H.) for the computational portion of the study. The authors are thankful to the Welch Foundation for its generous support through Grants F-1436 (C. B. M.) and F-1841 (G. H.). Computational resources were provided by the Texas Advanced Computing Center (TACC) and the National Energy Research Scientific Computing Center (NERSC). The authors are also grateful to the 3D printing services of the UACH's Innovation and Technological Entrepreneurship Center, particularly the help of Mr. Fernando Ledezma Millán. Additionally, R. A. A. M. (CVU 919871) wishes to thank CONACYT for his master's scholarship award as well as the Mexican Ministry of Foreign Relations (SRE) and the Consulate of Mexico in Austin for the Matías Romero Visiting Scholars Program. This research was also supported by the Basic Science Research Program through the National Research Foundation of Korea (NRF) funded by the Ministry of Education (No. 2019R1I1A3A01052741)

(D. H. Y.). Finally, the authors thank Dr. Hugo Celio for his kind assistance with XPS measurements.

References

1 M. T. M. Koper, *J. Electroanal. Chem.*, 2011, **660**, 254–260.
2 B. R. Wygant, K. Kawashima and C. B. Mullins, *ACS Energy Lett.*, 2018, **3**, 2956–2966.
3 K. N. Dinh, Q. Liang, C.-F. Du, J. Zhao, A. I. Y. Tok, H. Mao and Q. Yan, *Nano Today*, 2019, **25**, 99–121.
4 J. Joo, T. Kim, J. Lee, S.-I. Choi and K. Lee, *Adv. Mater.*, 2019, **31**, 1806682.
5 W. Li, D. Xiong, X. Gao and L. Liu, *Chem. Commun.*, 2019, **55**, 8744–8763.
6 Y. Li, X. Du, J. Huang, C. Wu, Y. Sun, G. Zou, C. Yang and J. Xiong, *Small*, 2019, **15**, 1901980.
7 J. Masa and W. Schuhmann, *ChemCatChem*, 2019, **11**, 5842–5854.
8 A. Sivanantham, P. Ganesan, A. Vinu and S. Shanmugam, *ACS Catal.*, 2019, 463–493.
9 Z. Chen, X. Duan, W. Wei, S. Wang, Z. Zhang and B.-J. Ni, *Nano Res.*, 2020, **13**, 293–314.
10 J. Masud, S. Umapathi, N. Ashokaan and M. Nath, *J. Mater. Chem. A*, 2016, **4**, 9750–9754.
11 A. T. Swesi, J. Masud and M. Nath, *Energy Environ. Sci.*, 2016, **9**, 1771–1782.
12 U. D. Silva, J. Masud, N. Zhang, Y. Hong, W. P. R. Liyanage, M. A. Zaeem and M. Nath, *J. Mater. Chem. A*, 2018, **6**, 7608–7622.
13 F. Guo, Y. Wu, H. Chen, Y. Liu, L. Yang, X. Ai and X. Zou, *Energy Environ. Sci.*, 2019, **12**, 684–692.
14 J.-H. Kim, K. Kawashima, B. R. Wygant, O. Mabayoje, Y. Liu, J. H. Wang and C. B. Mullins, *ACS Appl. Energy Mater.*, 2018, **1**, 5145–5150.
15 T. Liu, M. Li, X. Bo and M. Zhou, *ACS Sustainable Chem. Eng.*, 2018, **6**, 11457–11465.
16 X. Xu, C. Li, J. G. Lim, Y. Wang, A. Ong, X. Li, E. Peng and J. Ding, *ACS Appl. Mater. Interfaces*, 2018, **10**, 30273–30282.
17 O. Mabayoje, A. Shoola, B. R. Wygant and C. B. Mullins, *ACS Energy Lett.*, 2016, **1**, 195–201.
18 W. Chen, Y. Liu, Y. Li, J. Sun, Y. Qiu, C. Liu, G. Zhou and Y. Cui, *Nano Lett.*, 2016, **16**, 7588–7596.
19 B. R. Wygant, A. H. Poterek, J. N. Burrow and C. B. Mullins, *ACS Appl. Mater. Interfaces*, 2020, **12**, 20366–20375.
20 K. Kawashima, C. L. Cao, H. Li, R. A. Márquez-Montes, B. R. Wygant, Y. J. Son, J. V. Guerrera, G. Henkelman and C. B. Mullins, *ACS Sustainable Chem. Eng.*, 2020, **8**, 14101–14108.
21 X. Xu, F. Song and X. Hu, *Nat. Commun.*, 2016, **7**, 1–7.
22 M. Shalom, D. Ressnig, X. Yang, G. Clavel, T. P. Fellinger and M. Antonietti, *J. Mater. Chem. A*, 2015, **3**, 8171–8177.
23 K. Xu, P. Chen, X. Li, Y. Tong, H. Ding, X. Wu, W. Chu, Z. Peng, C. Wu and Y. Xie, *J. Am. Chem. Soc.*, 2015, **137**, 4119–4125.
24 Q. Zhang, Y. Wang, Y. Wang, A. M. Al-Enizi, A. A. Elzatahry and G. Zheng, *J. Mater. Chem. A*, 2016, **4**, 5713–5718.
25 M. Chen, J. Qi, D. Guo, H. Lei, W. Zhang and R. Cao, *Chem. Commun.*, 2017, **53**, 9566–9569.
26 B. Ouyang, Y. Zhang, Z. Zhang, H. J. Fan and R. S. Rawat, *Small*, 2017, **13**, 1604265.
27 J. Huang, Y. Li, Y. Zhang, G. Rao, C. Wu, Y. Hu, X. Wang, R. Lu, Y. Li and J. Xiong, *Angew. Chem., Int. Ed.*, 2019, **58**, 17458–17464.
28 Y. Zhang, B. Ouyang, J. Xu, G. Jia, S. Chen, R. S. Rawat and H. J. Fan, *Angew. Chem., Int. Ed.*, 2016, **55**, 8670–8674.
29 Y. Yan, B. Y. Xia, X. Ge, Z. Liu, A. Fisher and X. Wang, *Chem. – Eur. J.*, 2015, **21**, 18062–18067.
30 C.-C. Hou, S. Cao, W.-F. Fu and Y. Chen, *ACS Appl. Mater. Interfaces*, 2015, **7**, 28412–28419.
31 J. Chang, Y. Xiao, M. Xiao, J. Ge, C. Liu and W. Xing, *ACS Catal.*, 2015, **5**, 6874–6878.
32 L.-A. Stern, L. Feng, F. Song and X. Hu, *Energy Environ. Sci.*, 2015, **8**, 2347–2351.
33 A. Han, H. Chen, Z. Sun, J. Xu and P. Du, *Chem. Commun.*, 2015, **51**, 11626–11629.
34 A. Valizadeh and M. M. Najafpour, *New J. Chem.*, 2020, **44**, 19630–19641.
35 M. Ledendecker, S. Krick Calderón, C. Papp, H.-P. Steinrück, M. Antonietti and M. Shalom, *Angew. Chem., Int. Ed.*, 2015, **54**, 12361–12365.
36 J. Masa, S. Piontek, P. Wilde, H. Antoni, T. Eckhard, Y.-T. Chen, M. Muhler, U.-P. Apfel and W. Schuhmann, *Adv. Energy Mater.*, 2019, **9**, 1900796.
37 L. Trotochaud, S. L. Young, J. K. Ranney and S. W. Boettcher, *J. Am. Chem. Soc.*, 2014, **136**, 6744–6753.
38 M. B. Stevens, C. D. M. Trang, L. J. Enman, J. Deng and S. W. Boettcher, *J. Am. Chem. Soc.*, 2017, **139**, 11361–11364.
39 S. Klaus, Y. Cai, M. W. Louie, L. Trotochaud and A. T. Bell, *J. Phys. Chem. C*, 2015, **119**, 7243–7254.
40 D. Friebel, M. W. Louie, M. Bajdich, K. E. Sanwald, Y. Cai, A. M. Wise, M.-J. Cheng, D. Sokaras, T.-C. Weng, R. Alonso-Mori, R. C. Davis, J. R. Bargar, J. K. Nørskov, A. Nilsson and A. T. Bell, *J. Am. Chem. Soc.*, 2015, **137**, 1305–1313.
41 S. Lee, L. Bai and X. Hu, *Angew. Chem.*, 2020, **132**, 8149–8154.
42 M. Jiang, Y. Li, Z. Lu, X. Sun and X. Duan, *Inorg. Chem. Front.*, 2016, **3**, 630–634.
43 S. Nandi, S. K. Singh, D. Mullangi, R. Illathvalappil, L. George, C. P. Vinod, S. Kurungot and R. Vaidhyanathan, *Adv. Energy Mater.*, 2016, **6**, 1601189.
44 X. Jia, Y. Zhao, G. Chen, L. Shang, R. Shi, X. Kang, G. I. N. Waterhouse, L.-Z. Wu, C.-H. Tung and T. Zhang, *Adv. Energy Mater.*, 2016, **6**, 1502585.
45 Y. Fan, S. Ida, A. Staykov, T. Akbay, H. Hagiwara, J. Matsuda, K. Kaneko and T. Ishihara, *Small*, 2017, **13**, 1700099.
46 Z. Yin, Y. Sun, C. Zhu, C. Li, X. Zhang and Y. Chen, *J. Mater. Chem. A*, 2017, **5**, 13648–13658.
47 S. Zhao, M. Li, M. Han, D. Xu, J. Yang, Y. Lin, N.-E. Shi, Y. Lu, R. Yang, B. Liu, Z. Dai and J. Bao, *Adv. Funct. Mater.*, 2018, **28**, 1706018.
48 C. Zhu, A.-L. Wang, W. Xiao, D. Chao, X. Zhang, N. H. Tiep, S. Chen, J. Kang, X. Wang, J. Ding, J. Wang, H. Zhang and H. J. Fan, *Adv. Mater.*, 2018, **30**, 1705516.
49 G. He, X. Han, B. Moss, Z. Weng, S. Gadipelli, F. Lai, A. G. Kafizas, D. J. L. Brett, Z. X. Guo, H. Wang and I. P. Parkin, *Energy Storage Mater.*, 2018, **15**, 380–387.

50 A. Wu, Y. Xie, H. Ma, C. Tian, Y. Gu, H. Yan, X. Zhang, G. Yang and H. Fu, *Nano Energy*, 2018, **44**, 353–363.
51 C. Ray, S. C. Lee, B. Jin, A. Kundu, J. H. Park and S. C. Jun, *J. Mater. Chem. A*, 2018, **6**, 4466–4476.
52 A. Saad, Z. Cheng, X. Zhang, S. Liu, H. Shen, T. Thomas, J. Wang and M. Yang, *Adv. Mater. Interfaces*, 2019, **6**, 1900960.
53 X. Wang, Q. Li, P. Shi, J. Fan, Y. Min and Q. Xu, *Small*, 2019, **15**, 1901530.
54 M. Lv, Y. Zhou, S. A. Rasaki, H. Shen, C. Wang, W. Song, T. Thomas, M. Yang and J. Wang, *ChemElectroChem*, 2019, **6**, 5744–5749.
55 X. Liu, X. Lv, P. Wang, Q. Zhang, B. Huang, Z. Wang, Y. Liu, Z. Zheng and Y. Dai, *Electrochim. Acta*, 2020, **333**, 135488.
56 A. Saad, H. Shen, Z. Cheng, R. Arbi, B. Guo, L. S. Hui, K. Liang, S. Liu, J. P. Attfield, A. Turak, J. Wang and M. Yang, *Nano-Micro Lett.*, 2020, **12**, 79.
57 R. A. Márquez-Montes, K. Kawashima, K. M. Vo, D. Chávez-Flores, V. H. Collins-Martínez, C. B. Mullins and V. H. Ramos-Sánchez, *Environ. Sci. Technol.*, 2020, **54**, 12511–12520.
58 L. F. Arenas, F. C. Walsh and C. P. de León, *ECS J. Solid State Sci. Technol.*, 2015, **4**, P3080.
59 B. He, Y. Kuang, Z. Hou, M. Zhou and X. Chen, *J. Mater. Res.*, 2018, **33**, 213–224.
60 K. Kawashima, K. Shin, B. R. Wygant, J.-H. Kim, C. L. Cao, J. Lin, Y. J. Son, Y. Liu, G. Henkelman and C. B. Mullins, *ACS Appl. Energy Mater.*, 2020, **3**, 3909–3918.
61 G. Sun, J. Kürti, P. Rajczy, M. Kertesz, J. Hafner and G. Kresse, *THEOCHEM*, 2003, **624**, 37–45.
62 J. Hafner, *J. Comput. Chem.*, 2008, **29**, 2044–2078.
63 P. E. Blöchl, *Phys. Rev. B*, 1994, **50**, 17953–17979.
64 W. Kohn and L. J. Sham, *Phys. Rev.*, 1965, **140**, A1133.
65 J. P. Perdew, K. Burke and M. Ernzerhof, *Phys. Rev. Lett.*, 1996, **77**, 3865–3868.
66 H. Monkhorst and J. Pack, *Phys. Rev. B*, 1976, **13**, 5188–5192.
67 A. Buttler and H. Spliethoff, *Renewable Sustainable Energy Rev.*, 2018, **82**, 2440–2454.
68 R. A. Márquez-Montes, V. H. Collins-Martínez, I. Pérez-Reyes, D. Chávez-Flores, O. A. Graeve and V. H. Ramos-Sánchez, *ACS Sustainable Chem. Eng.*, 2020, **8**, 3896–3905.
69 K. Kawashima, M. Hojamberdiev, H. Wagata, K. Yubuta, S. Oishi and K. Teshima, *Cryst. Growth Des.*, 2015, **15**, 333–339.
70 N. Weidler, J. Schuch, F. Knaus, P. Stenner, S. Hoch, A. Maljusch, R. Schäfer, B. Kaiser and W. Jaegermann, *J. Phys. Chem. C*, 2017, **121**, 6455–6463.
71 J.-H. Kim, D. H. Youn, K. Kawashima, J. Lin, H. Lim and C. B. Mullins, *Appl. Catal., B*, 2018, **225**, 1–7.
72 K. Kawashima, M. Hojamberdiev, H. Wagata, K. Yubuta, K. Domen and K. Teshima, *ACS Sustainable Chem. Eng.*, 2017, **5**, 232–240.
73 R. L. Doyle, I. J. Godwin, M. P. Brandon and M. E. G. Lyons, *Phys. Chem. Chem. Phys.*, 2013, **15**, 13737–13783.
74 Y. Mao, B. Zhou and S. Peng, *J. Mater. Sci.: Mater. Electron.*, 2020, **31**, 9457–9467.
75 F. Dionigi and P. Strasser, *Adv. Energy Mater.*, 2016, **6**, 1600621.
76 M. B. Stevens, L. J. Enman, A. S. Batchellor, M. R. Cosby, A. E. Vise, C. D. M. Trang and S. W. Boettcher, *Chem. Mater.*, 2017, **29**, 120–140.
77 C. Wei, S. Sun, D. Mandler, X. Wang, S. Z. Qiao and Z. J. Xu, *Chem. Soc. Rev.*, 2019, **48**, 2518–2534.
78 J. Deng, M. R. Nellist, M. B. Stevens, C. Dette, Y. Wang and S. W. Boettcher, *Nano Lett.*, 2017, **17**, 6922–6926.
79 C. Dette, M. R. Hurst, J. Deng, M. R. Nellist and S. W. Boettcher, *ACS Appl. Mater. Interfaces*, 2019, **11**, 5590–5594.
80 P. Oliva, J. Leonardi, J. F. Laurent, C. Delmas, J. J. Braconnier, M. Figlarz, F. Fievet and A. de Guibert, *J. Power Sources*, 1982, **8**, 229–255.
81 Y.-F. Li and A. Selloni, *ACS Catal.*, 2014, **4**, 1148–1153.
82 I. C. Man, H.-Y. Su, F. Calle-Vallejo, H. A. Hansen, J. I. Martínez, N. G. Inoglu, J. Kitchin, T. F. Jaramillo, J. K. Nørskov and J. Rossmeisl, *ChemCatChem*, 2011, **3**, 1159–1165.
83 M. W. Louie and A. T. Bell, *J. Am. Chem. Soc.*, 2013, **135**, 12329–12337.
84 R. D. L. Smith, M. S. Prévot, R. D. Fagan, S. Trudel and C. P. Berlinguette, *J. Am. Chem. Soc.*, 2013, **135**, 11580–11586.
85 D. A. Corrigan, *J. Electrochem. Soc.*, 1987, **134**, 377–384.
86 Y. J. Son, K. Kawashima, B. R. Wygant, C. H. Lam, J. N. Burrow, H. Celio, A. Dolocan, J. G. Ekerdt and C. B. Mullins, *ACS Nano*, 2021, **15**, 3468–3480.